



Achieving highly efficient pH-universal hydrogen evolution by superhydrophilic amorphous/crystalline Rh(OH)₃/NiTe coaxial nanorod array electrode

Huachuan Sun^a, Linfeng Li^a, Muhammad Humayun^a, Huaming Zhang^b, Yanan Bo^c, Xiang Ao^a, Xuefei Xu^a, Kun Chen^c, Kostya (Ken) Ostrikov^d, Kaifu Huo^a, Wenjun Zhang^e, Chundong Wang^{a,*}, Yujie Xiong^{c,*}

^a School of Optical and Electronic Information, Wuhan National Laboratory for Optoelectronics, Optics Valley Laboratory, Huazhong University of Science and Technology, Wuhan 430074, China

^b Key Laboratory of Nondestructive Testing, Ministry of Education, Nanchang Hangkong University, Nanchang 330063, China

^c School of Chemistry and Materials Science, University of Science and Technology of China, Hefei 230026, Anhui, China

^d School of Chemistry and Physics and Centre for Materials Science, Queensland University of Technology, Brisbane, Queensland 4000, Australia

^e Center of Super-Diamond and Advanced Films (COSDAF) & Department of Materials Science and Engineering, City University of Hong Kong, 83 Tat Chee Avenue, Kowloon, Hong Kong, China

ARTICLE INFO

Keywords:

Amorphous Rh(OH)₃ scabbards
Crystalline NiTe nanorods
PH-universal
Hydrogen evolution reaction
Aerophobic

ABSTRACT

Design of high-performance pH-universal electrocatalysts is critical to practical large-scale hydrogen generation as a carbon-neutral fuel, yet challenging. Herein, we report an unique motif with crystalline nickel tellurium nanorods enclosed by amorphous rhodium hydroxide (a-Rh(OH)₃/NiTe), formed through a hydrothermal synthesis and a subsequent chemical etching process, to address this challenge. The as-prepared a-Rh(OH)₃/NiTe cathode enables a current density of 100 mA cm⁻² with low overpotentials of 51, 109, and 64 mV for HER in alkaline, neutral and acidic media, respectively. As revealed by density functional theory (DFT) calculations, the electronic interactions between a-Rh(OH)₃ and NiTe enhance the performance of Rh active sites. More importantly, the motif possesses superhydrophilicity and aerophobicity features, which not only facilitates the access to electrolytes but also ensures the fast release of hydrogen bubbles, endowing the electrocatalyst with advanced pH-universal HER activity. This work provides insights for the design of highly efficient electrocatalysts for hydrogen evolution at both molecular and mesoscopic levels.

1. Introduction

The global energy crisis along with serious environmental issues motivates us to find a green and efficient alternative to the traditional fossil fuels [1,2]. Hydrogen (H₂) as a clean form of carbon free energy carrier has been regarded as a promising candidate for next-generation energy [3,4]. Water electrolysis via the renewable-electricity from solar and wind energy is a sustainable and proficient method for producing high-purity H₂, which has gained tremendous attention in recent years [5,6]. Thus far, Pt-based materials are the benchmark HER catalysts due to their favorable Gibbs free energy (ΔG) of H⁺ adsorption (ΔG_{H*} = -0.09 eV), but their practical applications are greatly limited by the high cost and unsatisfactory stability [7,8]. More importantly, Pt-based

catalysts show poor HER activities in non-acidic media (i.e., neutral and alkaline electrolytes), which are generally about 2–3 orders of magnitude lower compared with that measured in the acidic medium due to their sluggish kinetics of the water dissociation in neutral and alkaline solutions [9,10]. Hence, it is highly desirable to design and develop ideal electrocatalysts with high performance and excellent stability for HER in a wide pH range.

To date, various earth-abundant crystalline nanomaterials such as metal hydroxides, oxides [11], phosphides [12], nitrides [13,14], sulfides [15], borides [16], carbides [17,18], and selenides [19,20] have been explored aiming to replace the commercial Pt catalyst, which demonstrated considerable HER activity. Unfortunately, most of these catalysts are explored as efficient fromoters for the cleavage of H-OH

* Corresponding authors.

E-mail addresses: apcdwang@hust.edu.cn (C. Wang), yjxiong@ustc.edu.cn (Y. Xiong).

<https://doi.org/10.1016/j.apcatb.2022.121088>

Received 4 October 2021; Received in revised form 28 December 2021; Accepted 6 January 2022

Available online 7 January 2022

0926-3373/© 2022 Elsevier B.V. All rights reserved.

bonds, but they are inferior in converting the resulting adsorbed H_{ad} species to H_2 [21]. Thus the catalytic activities and stability of these non-noble metal catalysts are still unsatisfactory relative to those of the noble metals, which hindered their large scale practical applications. Recently, some cost-effective precious metals such as Ru, Ir and Pd have been widely studied for enhancing the non-acidic HER activity due to their favorable hydrogen bonding energy [22–26]. However, these precious metal catalysts are usually synthesized under high temperatures or high-pressure conditions, and their ordinary stability also limits future applications [27].

In order to enhance the intrinsic activity and stability while simultaneously reducing the cost of noble metal catalysts, combining precious metal with non-noble metal is an effective approach [28,29]. It is noteworthy that most reported electrocatalysts are crystalline materials without amorphous counterpart involved [30]. Compared with the mostly studied crystalline materials with long-range order, amorphous materials such as amorphous rhodium hydroxide ($a-Rh(OH)_3$) and amorphous nickel hydroxide ($a-Ni(OH)_2$) are generally atomic-scale with structural flexibility, in which their internal atoms arrangement is not periodic but only allow the local short-range order [31–33]. Due to its disorderly feature, numerous randomly oriented bonds are produced, which endows $a-Rh(OH)_3$ and $a-Ni(OH)_2$ catalysts surface with abundant defects and coordinated unsaturated sites, consequently improving the catalytic activity [33–35]. Furthermore, the exceptional structural and isotropic properties makes amorphous catalysts strongly resistant to corrosion, both in the acidic and alkaline media, and provide new insights into the search for extremely stable catalysts [30,36]. From another perspective, it suggests that nanoarray structure could facilitate the faster release of the as-produced gas bubbles from the catalyst surface, thereby speeding up the catalytic process occurring on the electrode [29,37]. Given these facts, the rod-like core shell-structured catalyst design based on amorphous/crystalline materials should be an attractive strategy for improving the activity and stability of the electrocatalysts for HER under harsh environments.

In this work, we develop a motif with crystalline nickel tellurium nanorods enclosed by amorphous rhodium hydroxide on nickel foam (termed as $a-Rh(OH)_3/NiTe$) via a two-step scheme to improve the activity and stability toward pH-universal HER. The $a-Rh(OH)_3/NiTe$ catalyst exhibits exceptional HER catalytic activity in alkaline, neutral and acidic media, surpassing mostly reported noble metal electrocatalysts. The experimental and DFT calculation results reveal that the Rh sites in the $a-Rh(OH)_3$ are the extremely active centers, while the rod-like NiTe core serves as a co-working catalyst for charge transfer, yielding the high HER performance. Furthermore, the intriguing superhydrophilicity and aerophobicity feature of $a-Rh(OH)_3/NiTe$ is another key factor for the remarkable catalytic activity, allowing the easy access of electrolyte and facilitating the fast removal of the produced gas bubbles.

2. Experimental section

2.1. Synthesis of NiTe precursors and $a-Rh(OH)_3/NiTe$ on nickel foam (NF)

The NiTe nanoarray precursor was in situ anchored on Ni foam following our previous approaches reported elsewhere [19], in which the pretreated NF served as both the substrate and Ni source. For preparation of $a-Rh(OH)_3/NiTe$, the as-prepared NiTe nanoarray precursor was immersed in a 20 mL $RhCl_3 \cdot xH_2O$ (1 mg/mL) aqueous solution. Then the solution with NiTe precursor was kept in dark for 24 h to ensure the chemical etching process successful. Subsequently, the fabricated $a-Rh(OH)_3/NiTe$ sample was collected and dried in vacuum at 60 °C overnight. For comparison, the NiTe nanoarray precursor was etched by 20 mL $RhCl_3 \cdot xH_2O$ aqueous solution with different concentrations of 0.15, 0.3, 0.4, 0.5, 1.0, 1.5, 2.0 and 3.0 mg/mL, and the corresponding $a-Rh(OH)_3/NiTe$ samples were marked as $a-Rh$

$(OH)_3/NiTe$ -0.15, $a-Rh(OH)_3/NiTe$ -0.3, $a-Rh(OH)_3/NiTe$ -0.4, $a-Rh(OH)_3/NiTe$ -0.5, $a-Rh(OH)_3/NiTe$ -1, $a-Rh(OH)_3/NiTe$ -1.5, $a-Rh(OH)_3/NiTe$ -2 and $a-Rh(OH)_3/NiTe$ -3, respectively. The sample $a-Rh(OH)_3/NiTe$ -1 was chosen for characterizations unless otherwise noted. For simplicity, $a-Rh(OH)_3/NiTe$ -1 is termed as $a-Rh(OH)_3/NiTe$ hereinafter. We also studied the effects of different temperatures on the formation of $a-Rh(OH)_3/NiTe$ nanoarrays. The $a-Rh(OH)_3/NiTe$ was annealed at different temperatures, which are labeled as $a-Rh(OH)_3/NiTe$ -X, where X represent the different annealing temperatures such as 250, 350, 550 and 700 °C. Correspondingly, the samples were labeled as $a-Rh(OH)_3/NiTe$ -250, $a-Rh(OH)_3/NiTe$ -300, $a-Rh(OH)_3/NiTe$ -350, $a-Rh(OH)_3/NiTe$ -450, $a-Rh(OH)_3/NiTe$ -550, $a-Rh(OH)_3/NiTe$ -600, $a-Rh(OH)_3/NiTe$ -700 and $a-Rh(OH)_3/NiTe$ -900, respectively.

2.2. Characterizations

X-ray diffraction (XRD; Philips, X'pertPro, Cu K α radiation) was employed to examine the crystal structure, and the 2θ of all samples were collected from 5° to 80°. Scanning electron microscopy (SEM) images and the corresponding energy-dispersive X-ray spectroscopy (EDS) information of all samples were collected on a Zeiss G300 (accelerating voltage of 3 kV). Transmission electron microscopy (TEM, FEI, Tecnai G2 F30), high-resolution TEM (HRTEM), high-angle annular dark-field scanning TEM (HAADF-STEM) were performed to further confirm the morphology and microstructure of $a-Rh(OH)_3/NiTe$. The X-ray photoelectron spectroscopy (XPS, Thermo Fisher Scientific Escalab 250 spectrometer), TEM EDS, and the corresponding element mapping were collected to analyze the surface chemical compositions of the catalysts.

2.3. Electrochemical measurement

The electrochemical tests were performed in a CHI 760E electrochemical workstation. The as-prepared $a-Rh(OH)_3/NiTe$ and NiTe were used as working electrodes, and a graphite rod served as the counter electrode. The Hg/HgO electrode worked as a reference electrode in alkaline media, while the saturated calomel electrode (SCE) was used as the reference electrode in neutral and acidic electrolytes. The HER performance of all catalysts was evaluated by linear sweep voltammetry (LSV) measurements, and all LSV curves were recorded at 2 mV s⁻¹ scan rate. Noteworthy, the cyclic voltammetry (CV) measurements were performed for over 50 cycles (with a scan rate of 50 mV s⁻¹) to attain a stable state before LSV evaluation. All potentials measured in alkaline media were calibrated to reversible hydrogen electrode (RHE) using the following equation: $E_{RHE} = E_{Hg/HgO} + 0.098 + 0.059 \times pH$, where the E_{RHE} is the potential referred to reversible hydrogen electrode (RHE) and $E_{Hg/HgO}$ is measured with the Hg/HgO reference electrode, and pH = 13.8. All potentials measured in neutral and acidic media were calibrated to reversible hydrogen electrode (RHE) as well. In order to make the electrochemical data in this work more credible, the saturated calomel electrode (SCE) converted to reverse hydrogen electrode (RHE) has been calibrated and $E_{RHE} = E_{SCE} + 0.658$ V in neutral, and $E_{RHE} = E_{SCE} + 0.257$ V in acidic, where the E_{RHE} is the potential referred to reversible hydrogen electrode (RHE) and E_{SCE} is measured with the calomel electrode reference electrode. All the electrochemical measurements were corrected with 95% iR compensation unless otherwise noted.

3. Results and discussion

3.1. Synthesis and structure characterizations

Fig. 1a presents the schematical process for preparation of $a-Rh(OH)_3/NiTe$. NiTe nanoarrays are first grown on the nickel foam (NF) through a hydrothermal method, in which NF acted as both Ni source and substrate and N_2H_4 served as a reducing agent to react with

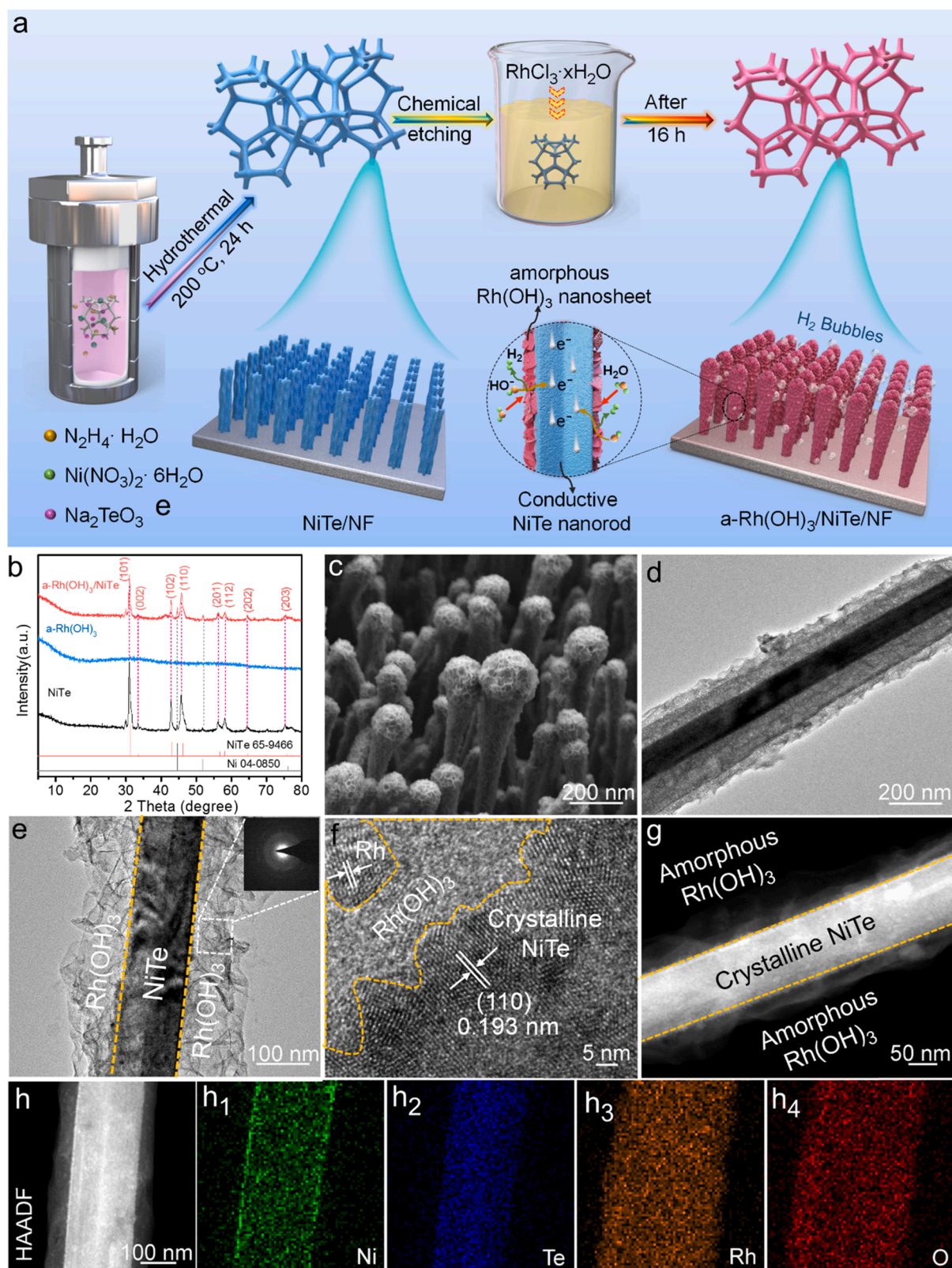


Fig. 1. Structural and morphological characterizations of a- $\text{Rh}(\text{OH})_3/\text{NiTe}$ electrode. **a)** Schematic illustration of the preparation process of a- $\text{Rh}(\text{OH})_3/\text{NiTe}$ supported on nickel foam. **b)** XRD patterns of bare NiTe and a- $\text{Rh}(\text{OH})_3/\text{NiTe}$. **c)** FESEM images of a- $\text{Rh}(\text{OH})_3/\text{NiTe}$. **d, e)** TEM images of a- $\text{Rh}(\text{OH})_3/\text{NiTe}$. Inset in **e** shows SAED patterns of amorphous $\text{Rh}(\text{OH})_3$. **f)** HRTEM images of a- $\text{Rh}(\text{OH})_3/\text{NiTe}$. **g, h)** HAADF-STEM images of a- $\text{Rh}(\text{OH})_3/\text{NiTe}$ with the corresponding elemental mapping images for Ni, Te, Rh, O elements.

Ni_2TeO_3 and Ni towards formation of NiTe. A combination of X-ray diffraction (XRD), scanning electron microscopy (SEM) and energy-dispersive X-ray spectroscopy (EDS) (Figs. S1 and S2) reveal that NiTe nanorods have been grown on NF surface. Subsequently, chemical etching was implemented in $\text{RhCl}_3 \cdot x\text{H}_2\text{O}$ aqueous solution, after which amorphous $\text{Rh}(\text{OH})_3$ layers were formed on NiTe nanorods surface. The etching preferentially occurred on the surface of NiTe nanorods with the assistance of Cl^- anions accelerating the corrosion process, leading to the in situ formation of amorphous $\text{Rh}(\text{OH})_3$ layers on the NiTe nanorods (Fig. S3) [38]. For comparison, the $\text{Rh}(\text{OH})_3$ powder was also prepared (Fig. S4a–c). XRD (Fig. 1b) suggests that the formed $\text{Rh}(\text{OH})_3$ is amorphous given that no additional diffraction peak is discerned compared with that of NiTe sample [39,40]. The amorphous nature of $\text{Rh}(\text{OH})_3$ could also be confirmed by the Fourier transform infrared (FT-IR) spectrum as one band centred at 545 cm^{-1} is identified (Fig. S4c) [39]. Furthermore, Raman spectroscopy was performed to obtain more chemical information of these electrocatalysts (Fig. S4d). Two similar bands were observed in both $\text{Rh}(\text{OH})_3$ and a- $\text{Rh}(\text{OH})_3/\text{NiTe}$, and the intensive Raman band centered at 450 and 538 cm^{-1} are associated with the symmetric Rh-OH stretching and/or structural defects [32,39,40]. As reported in literatures [32], the peak at 538 cm^{-1} is sensitive to defects of amorphous materials, again verifying that the formed $\text{Rh}(\text{OH})_3$ layer on NiTe is amorphous.

The chemical etching is a key step to form the desired nanostructures in our materials synthesis. SEM images (Figs. 1c and S3) show that the nanorod arrays are preserved after chemical etching except that the surface of NiTe nanorods becomes rough. Combined with EDS characterization, this suggests that amorphous $\text{Rh}(\text{OH})_3$ has been successfully grown on NiTe. For comparison, a series of control samples (Figs. S5–S11) are prepared, for which we can change the contents of a- $\text{Rh}(\text{OH})_3$ in the core-shell structures. We noticed that the morphology of a- $\text{Rh}(\text{OH})_3/\text{NiTe}$ samples become rougher with increasing the concentration of $\text{RhCl}_3 \cdot x\text{H}_2\text{O}$ aqueous solution. Among the samples, the optimum sample is the one with Rh content of 11.93 wt% (termed as a- $\text{Rh}(\text{OH})_3/\text{NiTe}$ -1), in which the deposited amorphous $\text{Rh}(\text{OH})_3$ layers are distributed uniformly on the NiTe nanorods. To verify the structure stability of the as-prepared a- $\text{Rh}(\text{OH})_3/\text{NiTe}$ -1, annealing treatment at different temperatures is carried out (Figs. S12–S18). As expected, the nanostructure morphology of a- $\text{Rh}(\text{OH})_3/\text{NiTe}$ -1 would be damaged when the temperature is elevated above 600°C , along with some oxidation of NiTe to NiO. When the annealing temperature is over 700°C , some RhO_2/NiTe or $\text{Rh}_2\text{O}_3/\text{Ni}_3\text{TeO}_6$ will also be formed (Figs. S18 and S19) [40,41]. These observations suggest that the amorphous/crystalline phase of a- $\text{Rh}(\text{OH})_3/\text{NiTe}$ -1 should be stable when the annealing temperature is below 600°C , manifesting the high stability of our catalyst.

The morphology of a- $\text{Rh}(\text{OH})_3/\text{NiTe}$ is further examined by transmission electron microscopy (TEM). A unique motif of crystalline nanorods stuffed into amorphous scabbards is discerned, in which the rod-like core is NiTe and the shell is the amorphous $\text{Rh}(\text{OH})_3$ (Figs. 1d, e and S20 and S21). The amorphous nature of the shell $\text{Rh}(\text{OH})_3$ is also confirmed by the high-resolution TEM (HRTEM) images and the selected-area electron diffraction (SAED) patterns (Fig. 1e) [36]. The lattice fringes with a spacing of 0.193 nm corresponds to the (110) plane of NiTe while the lattice spacing of 0.19 nm is assigned to the (200) facet of metal Rh (Fig. 1f) [23,42]. Since no peaks relevant to the Rh nanoparticles is observed in the XRD pattern (Fig. 1b), it suggests that the amount of metallic Rh is very small. Also, we collected SAED patterns, in which the explicit diffraction rings are indexed to (110), (102), (211), (203) and (212) planes of NiTe (Fig. S22) while no Rh fingerprint was discerned, further confirming that there is no obvious Rh nanoparticles on the shell.

After careful scrutiny, the interface between amorphous $\text{Rh}(\text{OH})_3$ and crystalline NiTe can be resolved (Fig. S21f). Impressively, the motif of crystalline nanorods enclosed with amorphous scabbards can be more easily identified from the corrected high-angle annular dark-field

scanning transmission electron microscope (HAADF-STEM) images (Figs. 1g and S23). The corresponding elemental mapping demonstrates that the Ni and Te elements are concentrated in the rod-like core of the nanorod, while Rh and O elements are distributed over the whole nanorods (Fig. 1h), verifying the fact that the NiTe nanorods are covered by the $\text{Rh}(\text{OH})_3$ amorphous layers, which is in line with the SEM and TEM results.

X-ray photoelectron spectroscopy (XPS) was recorded to unveil the valance states of a- $\text{Rh}(\text{OH})_3/\text{NiTe}$. In the XPS survey spectrum of NiTe (Fig. 2a), Ni 2p and Te 3d peaks are observed. In addition to Ni 2p and Te 3d peaks, additional Rh 3d and Rh 3p peaks can be identified after chemical etching, suggesting that the $\text{Rh}(\text{OH})_3$ has been grown on the surface of NiTe (Table S1, S2) [29,43]. In the core-level Ni 2p spectrum of NiTe (Fig. 2b), two pronounced peaks at 855.31 and 876.07 eV are assigned to Ni $2p_{3/2}$ and Ni $2p_{1/2}$, respectively, accompanied with two satellite peaks at 861.56 and 879.73 eV . These peaks correspond to the state of Ni^{2+} in NiTe [23,44]. Compared with the bare NiTe, both Ni $2p_{3/2}$ and Ni $2p_{1/2}$ peaks of a- $\text{Rh}(\text{OH})_3/\text{NiTe}$ are shifted toward higher binding energies, suggesting a strong electronic interaction between a- $\text{Rh}(\text{OH})_3$ and NiTe [42]. Such an observation is also discerned in Te 3d spectra. The peaks at 572.57 and 582.95 eV corresponds to $\text{Te}^{2-} 3d_{5/2}$ and $\text{Te}^{2-} 3d_{3/2}$, respectively (Fig. 2c) [23]. The satellite peaks in Te 3d with the binding energy of 575.95 and 586.43 eV may result from the oxidation of Te exposed in air [45]. Notably, the $3d_{5/2}$ and $3d_{3/2}$ of Te^{2-} for a- $\text{Rh}(\text{OH})_3/\text{NiTe}$ are shifted by 0.35 eV toward higher binding energy relative to those of the bare NiTe, signifying partial of the electrons depletion after a- $\text{Rh}(\text{OH})_3$ layer coating [42]. To further clarify the electronic interactions, the Rh 3d and O 1s core-level spectra were collected as well. As shown in Fig. 2d, the peaks located at 309.71 eV and 314.48 eV can be assigned to the Rh $3d_{5/2}$ and Rh $3d_{3/2}$ of Rh^{3+} , respectively [29,46]. The other two lower intensity peaks at 307.31 and 312.38 eV are attributed to the Rh $3d_{5/2}$ and Rh $3d_{3/2}$ of metallic Rh^0 [46]. Compared with Rh 3d of bare a- $\text{Rh}(\text{OH})_3$, both Rh $3d_{3/2}$ and Rh $3d_{5/2}$ of a- $\text{Rh}(\text{OH})_3/\text{NiTe}$ were negatively shifted by 0.45 eV , indicating that partial electrons were enriched in Rh and a small portion of trivalent rhodium has been reduced during the chemical etching process. These observations suggest that the interfacial charges were transferred from Ni and Te to Rh. In the meantime, the O 1s spectra of the a- $\text{Rh}(\text{OH})_3/\text{NiTe}$ also provide some key information. The two peaks located at 530.2 and 531.13 eV are respectively ascribed to the metal oxides (M-O) and RhO_xH_y species, and the other peak located at 532.05 eV are accredited to the O-H group of the chemisorbed water (Fig. S24) [30]. As compared with the O 1s of bare NiTe, the binding energy of O 1s in sample a- $\text{Rh}(\text{OH})_3/\text{NiTe}$ is lower and a significant enhancement in the peak area of RhO_xH_y species is identified. This clarifies that the defects in a- $\text{Rh}(\text{OH})_3/\text{NiTe}$ are filled with oxygen atoms, which are then transformed to OH species [30].

Upon recognizing this feature, we also refer to electron spin resonance (ESR) measurement to probe the unpaired electrons which were generated by defects (Fig. 2e). As expected, a pair of sharp peaks were observed in a- $\text{Rh}(\text{OH})_3/\text{NiTe}$ in comparison to the bare NiTe, validating the fact that a- $\text{Rh}(\text{OH})_3/\text{NiTe}$ possesses a large number of defects [30, 47]. It is noteworthy that the defective sites will not only affect the electron distribution but also combined with oxygen atoms toward the formation of RhO_xH_y species, boosting the reaction kinetics [30,48]. Given that the -band center has a close relationship with the adsorption strength of the hydrogen adsorption intermediate [49], we further carried out the surface valence band XPS measurement to assess the band center of all catalysts (Fig. 2f). Compared with the bare NiTe, the -band center of a- $\text{Rh}(\text{OH})_3/\text{NiTe}$ was slight shifted to the Fermi level, signifying that the binding strength of the hydrogenated species (H^*) is enhanced with $\text{Rh}(\text{OH})_3$ decoration [23,29,49]. This finding suggests that the a- $\text{Rh}(\text{OH})_3/\text{NiTe}$ has strong affinity for the hydrogen adsorbed species, which may facilitate the Tafel step in HER.

In addition to the catalytically active centers, surface property is another key factor for the addressed HER performance as gas-liquid-

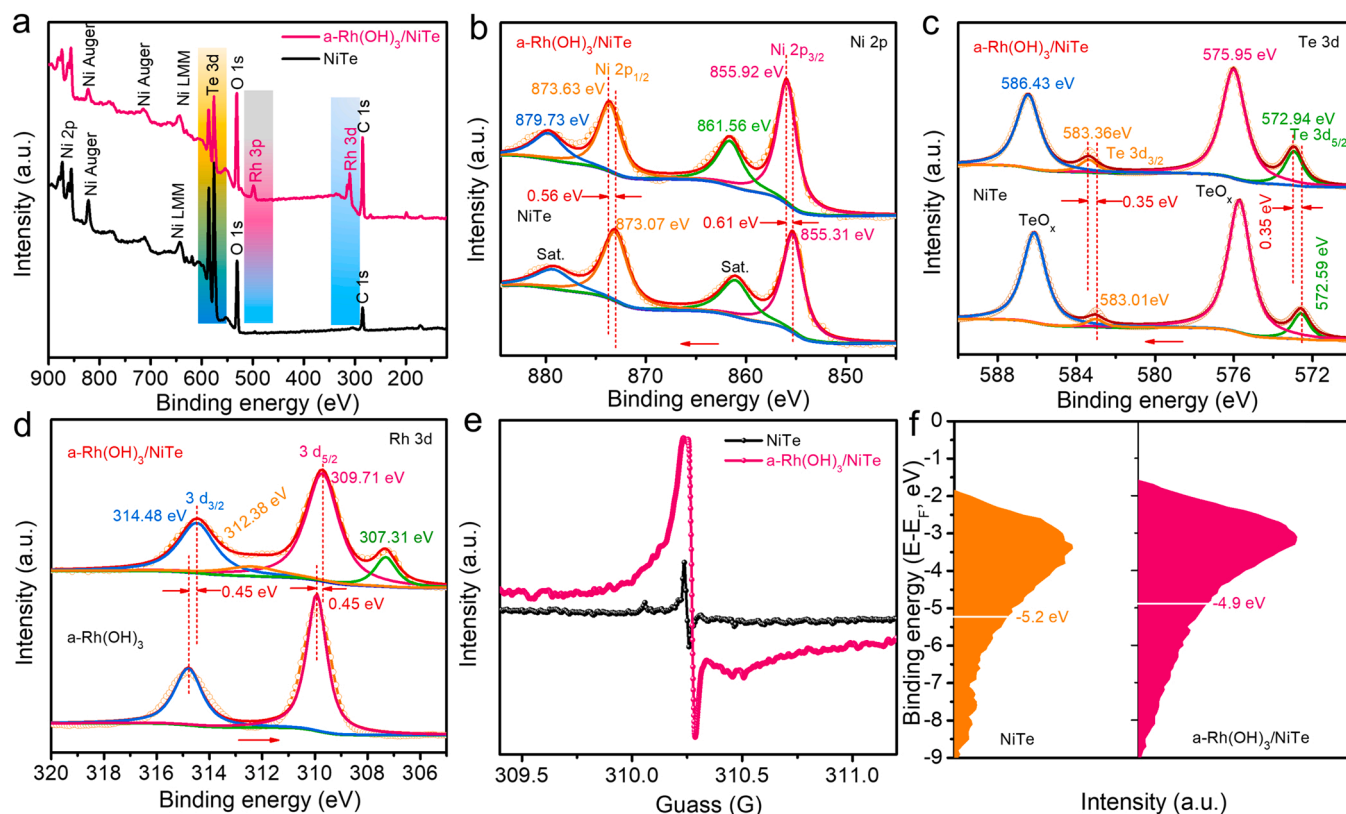


Fig. 2. Structure characterizations of a-Rh(OH)₃/NiTe electrode. a) XPS survey spectra of NiTe and a-Rh(OH)₃/NiTe. c-d) XPS spectra of the Ni 2p, Te 3d and Rh 3d. e) ESR spectra of NiTe and a-Rh(OH)₃/NiTe. f) Surface valence band XPS spectra of NiTe and a-Rh(OH)₃/NiTe.

solid triphase is extremely important for hydrogen generation process. To unveil the surface properties of a-Rh(OH)₃/NiTe, contact angles are measured in 1 M KOH alkaline solution. As shown in Fig. 3a, the droplets of KOH electrolyte are captured by the surface of bare NF and the angle is enlarged with time increase. After 5 s, the value of contact angle surpasses 115°, suggesting that the wetting ability of NF is poor. The insets 1'–3' in Fig. 3b–b2 show the static water-droplet behaviors. The expression 1' demonstrates the KOH solution droplets close to the a-Rh(OH)₃/NiTe electrode surface, while the expression 2' shows the interaction of KOH solution droplets with the electrode surface. Later on, the expression 3' displays that the droplets spread immediately when they comes in contact with the surface of a-Rh(OH)₃/NiTe nanoarrays, and the contact angle cannot be captured by the high-speed camera (Fig. 3b). These observations suggest that the as-prepared a-Rh(OH)₃/NiTe is superhydrophilic [50]. It should be noted that the electrode with superhydrophilicity feature favors an intimate contact between the electrode and electrolyte, which not only maximize surface active sites but also accelerate reaction kinetics [27,50].

In addition to the wettability, the underwater gas bubbles contact angles were also measured for the as-prepared electrode. As shown in Fig. 3c–e, the gas bubbles contact angles were measured to be 136, 155 and 166° for NF, NiTe and a-Rh(OH)₃/NiTe, respectively, indicating that the NiTe nanorods are more aerophobic than the bare NF. Since the amorphous Rh(OH)₃ can further improve the aerophobicity of NiTe, it is reasonable that a-Rh(OH)₃/NiTe is aerophobic. To better understand the “aerophobic” property of the as-prepared a-Rh(OH)₃/NiTe, the corresponding schematic diagram is provided as well (Fig. 3f). The schematic illustration shows that the produced H₂ bubbles are adhered onto the surface of bare NF, which then leads to a weak contact interface and limited electron transfer (Fig. 3f, left). This eventually cause poor HER performance. On the contrary, the “aerophobic” structure of NiTe and a-Rh(OH)₃/NiTe released the H₂ bubbles quickly (Fig. 3f, middle and right), Resulting in the steady contact between the catalytic sites and

electrolyte, which provide favorable conditions for HER [51]. This characteristic can be ascribed to the discontinuous state of the three phased contact-line (TPCL) of the bubbles within the hierarchically amorphous surface of the electrode that contributed to the extremely low contact region between the bubbles and electrode surface [37,51, 52]. Thus, the unique “superhydrophilic and aerophobic” property of the obtained Rh(OH)₃/NiTe also play a critical role in the remarkably improved HER catalytic activities.

3.2. HER performance

We are now in a position to assess the HER performance of a-Rh(OH)₃/NiTe and the control samples, performed in 1 M KOH electrolyte with a three-electrode configuration. To optimize the HER catalytic activity, we have prepared a series of a-Rh(OH)₃/NiTe samples by adjusting the RhCl₃·xH₂O amount for the chemical etching process. We recognize that with the increase of Rh(OH)₃ content, the XRD diffraction peaks of NiTe do not change while the crystallinity of a-Rh(OH)₃/NiTe is getting worse (Figs. S25a, and S3–S11). Accordingly, with the increase of Rh(OH)₃ content, the HER catalytic activity of a-Rh(OH)₃/NiTe in alkaline media gradually increases and finally decreases (Fig. S25). Among the samples, the optimal one is a-Rh(OH)₃/NiTe-1 with Rh loading amount of 11.93 wt%. The a-Rh(OH)₃/NiTe-1 is termed as a-Rh(OH)₃/NiTe as aforementioned unless otherwise noted.

To manifest the uniqueness of our design, we also measure the HER performance of Rh(OH)₃/NiTe annealed at different temperatures and other amorphous/crystalline heterostructures, such as a-Rh(OH)₃/NiSe, a-Rh(OH)₃/NiO, a-Rh(OH)₃/NiTe-NS and a-Ir(OH)₃/NiTe on NF, were also evaluated (Figs. S26–S34). Among all the samples, the fresh a-Rh(OH)₃/NiTe (without any annealing treatment) exhibits the best HER catalytic activity. In comparison, it was noticed that the sample annealed at 250 °C delivers advanced HER performance, nearly close to the fresh sample. Nonetheless, the catalytic activity decreased

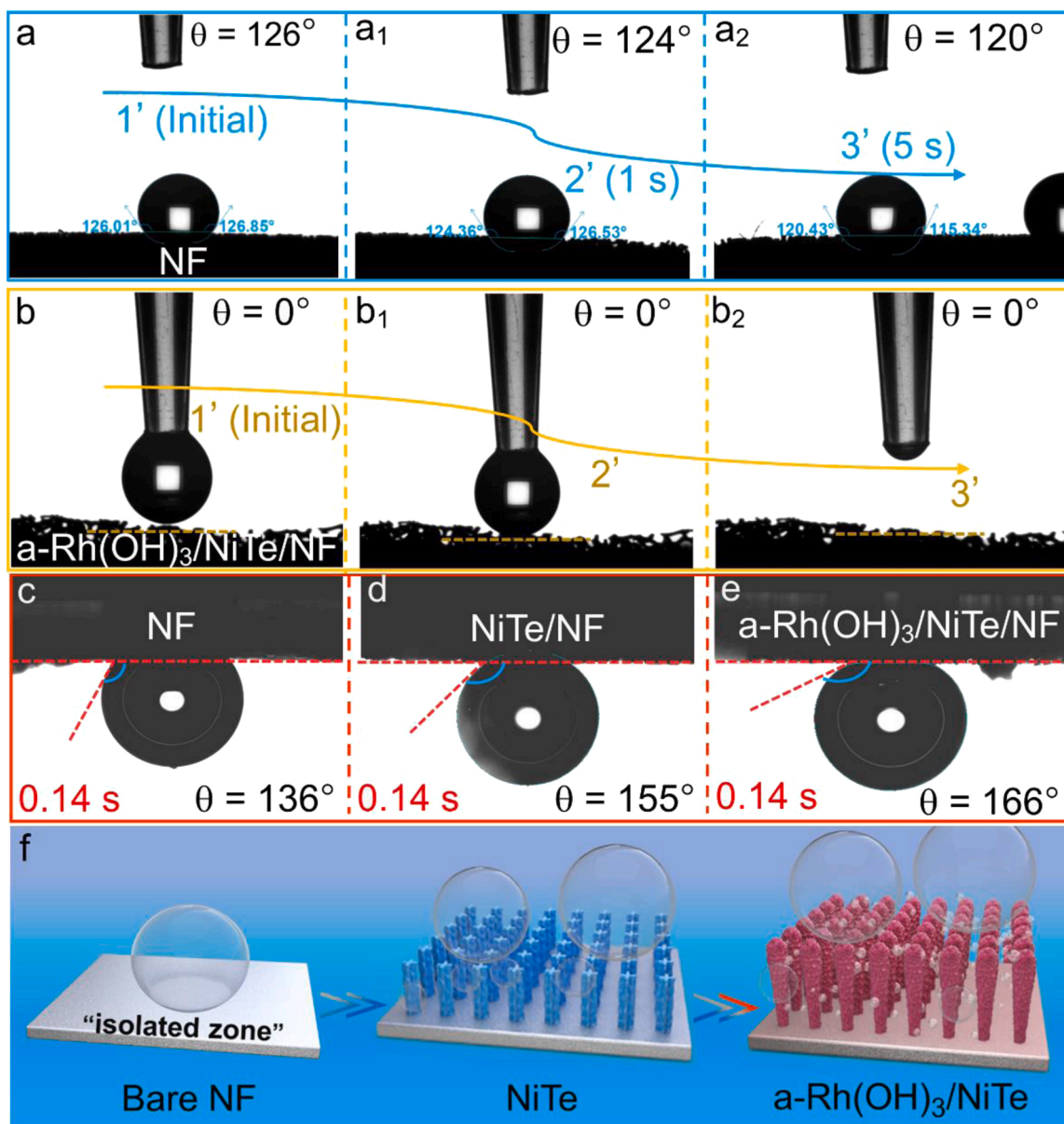


Fig. 3. Superhydrophilic and aerophobic measurements. a–b) The static droplets contact angles of bare NF and a-Rh(OH)₃/NiTe. The insets 1'–3' in a show the static-water-droplet measurement process where the KOH electrolyte droplets could be captured on the bare NF surface with passage of time. c–e) The air-bubble contact angles of bare NF, NiTe and a-Rh(OH)₃/NiTe under electrolyte. f) Schematic illustration of the adhesion behavior for a hydrogen molecule bubble on bare NF (left side), NiTe (middle) and a-Rh(OH)₃/NiTe nanoarrays (right side). The contact vicinity is an “isolated zone” ascribed to the bubble effect.

significantly with the annealing temperature increasing (Fig. S26). These catalytic behaviors suggest that the number of the coordinatively unsaturated sites (i.e. active sites) in the as-prepared a-Rh(OH)₃/NiTe was reduced as the amorphous Rh(OH)₃ layers converted to the counterpart crystalline rhodium oxides with temperature rising. Thus, it evidences the fact that the amorphous Rh(OH)₃ shells have a critical effect for addressing the enhanced HER activity.

As expected, the polarization curves shown in Figs. 4a and S34a presents that the a-Rh(OH)₃/NiTe affords the highest HER activity as compared with other amorphous/crystalline heterostructures. Impressively, the a-Rh(OH)₃/NiTe only needs an overpotential of 9 mV to attain a current density of 10 mA cm^{-2} , while the commercial Pt/C, a-Rh(OH)₃/NiSe, a-Rh(OH)₃/NiTe-NS, a-Rh(OH)₃/NiO, a-Ir(OH)₃/NiTe, and NiTe require overpotentials of 25, 21, 29, 31, 134 and 177 mV, respectively (Figs. 4b and S34b). Moreover, to research a high current density of 200 mA cm^{-2} , the a-Rh(OH)₃/NiTe only requires an overpotential of 85 mV, which is substantially lower than that of the

commercial Pt/C (126 mV). Such a performance surpasses most of the HER catalysts reported so far (Table S3). The remarkable activity of the configured amorphous/crystalline Rh(OH)₃/Ni-M (M represents O, Se, Te) evidences that the advanced catalytic activity should be attributed to the synergistic effect of the interfaces and the amorphous feature of the Rh(OH)₃ shells [21,23]. It should be acknowledged that the pure Ni-M generally shows poor HER catalytic activity as compared with the a-Rh(OH)₃/Ni-M heterostructure. However, the Ni-M provide a substrate for a-Rh(OH)₃ and improve the electrical conductivity of the whole sample (i.e., the amorphous/crystalline heterostructure) when the Ni-M are combined with a-Rh(OH)₃, which should be the reason for the advanced HER activity of the Rh(OH)₃/Ni-M samples. We thus believe that the unique motif of crystalline nanorods stuffed into amorphous scabbards, where the amorphous a-Rh(OH)₃ layers improve the adsorption of reaction intermediates and the crystalline NiTe nanorods facilitate electron transfer [24], should be the key to achieving high HER performance.

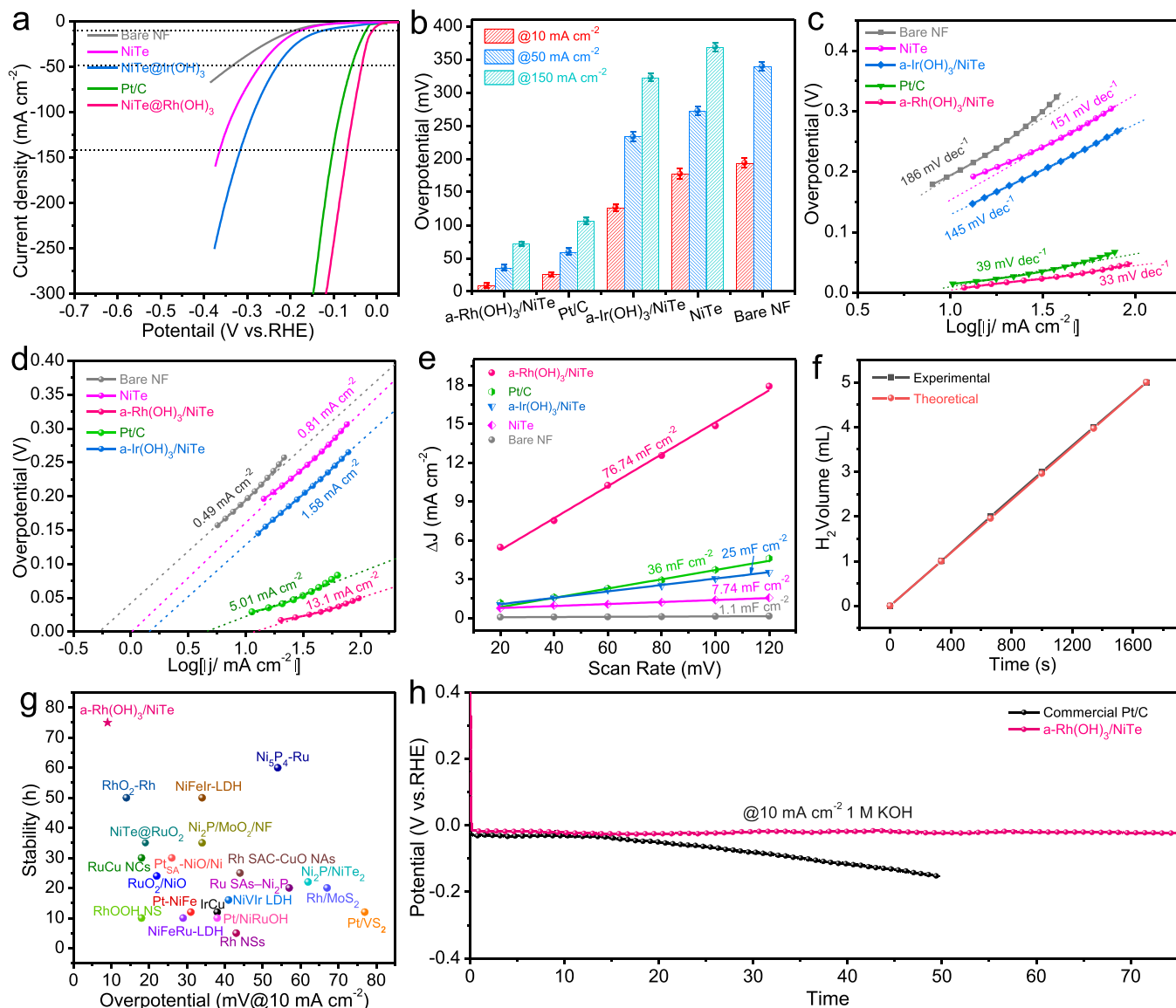


Fig. 4. Electrocatalytic HER performance in 1 M KOH solution. a) Polarization curves of the electrocatalysts for HER (with iR compensation). b) The resultant overpotentials at current densities of 10, 50 and 150 mA cm⁻² for the as-prepared electrocatalysts. c) The corresponding Tafel plots. d) Exchange current densities of the electrocatalysts. e) Extraction of the electrochemical double-layer capacitances (C_{dl}) from different electrodes. f) Comparison of the evolved hydrogen volume with the theoretical hydrogen volume calculated based on the amount of consumed charges over the course of electrolysis. g) Comparison of the catalytic activity and stability for a-Rh(OH)₃/NiTe with other reported catalysts, originating from Table S3. h) The chronopotentiometry tests of a-Rh(OH)₃/NiTe and Pt/C in 1 M KOH at 10 mA cm⁻².

To elucidate the reaction kinetics of the as-prepared electrocatalysts, Tafel slopes are calculated. As revealed in Fig. 4c, the Tafel slope of a-Rh(OH)₃/NiTe catalyst is 33 mV dec⁻¹, comparatively smaller than those of the bare NiTe (151 mV dec⁻¹) and the commercial Pt/C (39 mV dec⁻¹). Noteworthy, the Tafel slope value of a-Rh(OH)₃/NiTe is also lower than those of a-Rh(OH)₃/NiSe (53 mV dec⁻¹), a-Rh(OH)₃/NiTeNS (71 mV dec⁻¹), a-Ir(OH)₃/NiTe (131 mV dec⁻¹), and a-Rh(OH)₃/NiO (145 mV dec⁻¹) (Fig. S34c). Therefore, the a-Rh(OH)₃/NiTe electrode possesses the best reaction kinetics as compared with the other electrocatalysts. The small Tafel slope signifies that the HER process follows a Volmer Tafel pathway ($* + \text{H}_2\text{O} + \text{e}^- \rightarrow \text{H}_{\text{ads}} + \text{OH}^-$, $\text{H}_{\text{ads}} + \text{H}_{\text{ads}} \rightarrow 2* + \text{H}_2$), in which the rate-limiting step is the second one [23,27]. Furthermore, the exchange current density (j_0) of the electrocatalysts was determined by extrapolating the intercept of the Tafel plots at the zero overpotential (Fig. 4d). The j_0 value of a-Rh(OH)₃/NiTe is determined to be 13.1 mA cm⁻², which is 2.6 and 16.2 times higher than that of the Pt/C and NiTe, respectively. This indicates that the constructed

amorphous/crystalline Rh(OH)₃/NiTe interface could enhance the electron transfer rate and the intrinsic electrocatalytic HER activities. Nevertheless, the j_0 value of a-Rh(OH)₃/NiTe catalyst is also larger than those of a-Rh(OH)₃/NiSe (10 mA cm⁻²) and a-Rh(OH)₃/NiO (4.47 mA cm⁻²) (Fig. S34d).

The information gleaned above indicates that the interface of a-Rh(OH)₃ with NiTe performs better than others. In fact, the metalloid Te presents higher electronic conductivity as compared with the other chalcogenides (such as Se and O) [23,45,53,54]. To prove our assumption, electrochemical impedance spectra (EIS) are measured to explore the electron transfer kinetics. Figs. S34e and S35a show the Nyquist plots of the electrocatalysts, which were fitted according to the equivalent-circuit model (Fig. S35b). The charge transfer resistance (R_{ct}) of a-Rh(OH)₃/NiTe is determined to be about 0.9 Ω, which is smaller than those of the Pt/C (1.3 Ω), a-Rh(OH)₃/NiSe (1.4 Ω), a-Ir(OH)₃/NiTe (2.4 Ω), a-Rh(OH)₃/NiO (3.2 Ω), and bare NiTe (11.3 Ω). This result manifests the fact that the a-Rh(OH)₃/NiTe has the smallest charge

transfer resistance. Moreover, the j_0 value of NiTe is larger than that of the bare NF, which confirms that the crystalline rod-like core of NiTe nanorods can facilitate the transfer of electrons and improve the electrical conductivity [53].

To further elucidate the HER performance of a-Rh(OH)₃/NiTe, the electrochemical double layer capacitance (C_{dl}) of the electrode was measured to predict the electrochemically-active surface areas (ECSA). As revealed in Figs. 4e, S36 and S34f, a-Rh(OH)₃/NiTe exhibits the largest C_{dl} value of 76.74 mF cm⁻², in comparison with Pt/C (36 mF cm⁻²), a-Rh(OH)₃/NiTe NS (58.66 mF cm⁻²), a-Rh(OH)₃/NiSe (61.14 mF cm⁻²), a-Ir(OH)₃/NiTe (25 mF cm⁻²), a-Rh(OH)₃/NiO (25.94 mF cm⁻²), and bare NiTe (7.74 mF cm⁻²). Hence, it is found that the ECSA of a-Rh(OH)₃/NiTe is 1279 cm², significantly larger than those of Pt/C (600 cm²), a-Rh(OH)₃/NiTe NS (977.67 cm²), a-Rh(OH)₃/NiSe (1027.33 cm²) and NiTe (129 cm²), informing that our as-prepared core of crystalline nanorods wrapped by amorphous layer shell can expose more active sites for HER (Fig. S37a). To further disclose the intrinsic HER activities, the linear sweep voltammetry LSV curves normalized to ECSA are recorded. As revealed in Fig. S37b, the electrocatalytic activity of a-Rh(OH)₃/NiTe is still better than that of Pt/C, a-Rh(OH)₃/NiTe NS,

a-Rh(OH)₃/NiSe, and a-Ir(OH)₃/NiTe, even when the surface area effect is considered, revealing that the amorphous/crystalline interface in Rh(OH)₃/NiTe is the contributor for the advanced HER activity [28,53]. Impressively, we noticed that the measured Faraday efficiency of Rh(OH)₃/NiTe electrode for HER is close to 100% (Fig. 4f), verifying the fact that no other side reaction occur during catalysis process [55].

In addition to the excellent electrocatalytic HER activity, long-term stability is another key factor for practical applications. To this end, the stability feature was also evaluated. As shown in Fig. S37c, due to its binder-free and self-supporting characteristics, the LSV curves of a-Rh(OH)₃/NiTe shows little decrease after 3000 CV cycles, confirming its outstanding stability. Furthermore, chronopotentiometry measurement was also conducted to assess the durability of our as-prepared a-Rh(OH)₃/NiTe. As expected, no significant decline was discerned after 75 h continuous working, evidencing the fact that our as-prepared catalyst is more stable than both the commercial Pt/C and most reported catalysts (Fig. 4g, h and Table S3). The structural and compositional stability of a-Rh(OH)₃/NiTe are further confirmed by SEM, TEM, XRD and XPS characterizations (Figs. S38, 39).

Encouraged by the beneficial physicochemical and electrocatalytic

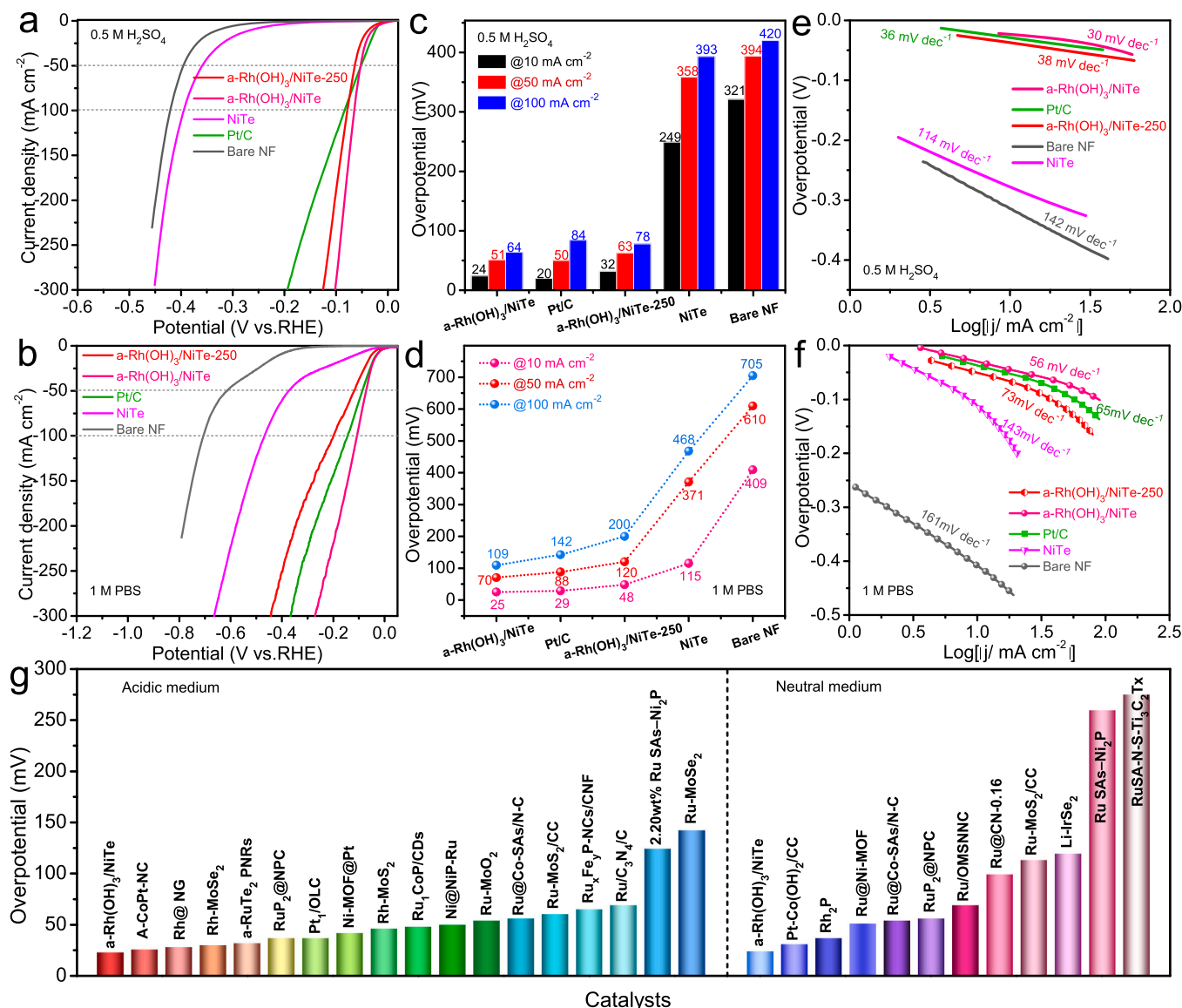


Fig. 5. Electrochemical studies of catalysts in acidic and neutral electrolytes. a, b) HER polarization curves of a-Rh(OH)₃/NiTe, a-Rh(OH)₃/NiTe-250, NiTe, Pt/C and bare NF in 0.5 M H₂SO₄ and 1 M PBS, respectively. c, d) The derived overpotentials at 10, 50 and 100 mA cm⁻² for the as-prepared catalysts. e, f) The Tafel plots. g) A comparison between the a-Rh(OH)₃/NiTe and the reported noble-metal based HER catalysts under different pH conditions, originating from Tables S4 and S5.

uniqueness of a-Rh(OH)₃/NiTe, we further explore whether our a-Rh(OH)₃/NiTe can serve as a pH-universal electrocatalyst for HER. Thus we evaluated the HER performance of a-Rh(OH)₃/NiTe in acidic and neutral medium (Figs. 5a, b and S40). It turns out that the excellent catalytic activity is achieved for the a-Rh(OH)₃/NiTe heterostructure with the low overpotential of 64 and 109 mV to achieve 100 mA cm⁻² in 0.5 M H₂SO₄ and 1 M phosphate buffered saline (PBS) solution, respectively (Fig. 5c and d). Note that the optimal HER performance of a-Rh(OH)₃/NiTe is significantly higher than that of a-Rh(OH)₃/NiTe-250 and NiTe, and even outperforms the state-of-the-art Pt/C with the applied voltage increasing (Fig. 5a–d). Apart from the overpotential, the corresponding Tafel slopes of the a-Rh(OH)₃/NiTe electrode in acidic and neutral medium are determined to be 30 and 56 mV dec⁻¹, respectively, which are smaller than that of the commercial Pt/C (Fig. 5e and f), suggesting the a-Rh(OH)₃/NiTe catalyst can maintain its faster reaction kinetics during the HER process even in acidic and neutral media. Furthermore, the robust structure stability of a-Rh(OH)₃/NiTe in acidic and neutral conditions is evaluated by implementing the accelerated degradation experiments (Fig. S41). The structure and morphology of a-Rh(OH)₃/NiTe after the stability test was studied by the XRD, SEM and EDS characterizations (Figs. S42, S43). Compared with the reported noble-metal based HER catalysts in strongly acidic and neutral conditions, the a-Rh(OH)₃/NiTe electrode also presents superior HER activity (Fig. 5g, Tables S4 and S5). Remarkably, the a-Rh(OH)₃/NiTe can be used as a highly-efficient HER electrocatalyst at a wide pH range.

3.3. Mechanistic study

To fundamentally decode the mechanism for the advanced HER activity of a-Rh(OH)₃/NiTe, DFT calculations are performed to study the electronic structure and H₂O adsorption energy ΔE (H₂O) as well as the atomic hydrogen adsorption energy (ΔG_{H^+}). In more detail, hexagonal NiTe (P6₃/mmc) and amorphous rhodium hydroxide (a-Rh(OH)₃) were chosen as the models for calculation. Unfortunately, a-Rh(OH)₃ is long-range disorder and no standard atom model of a-Rh(OH)₃ is reported yet. Thus, it is difficult to build a precise model for simulating a-Rh(OH)₃ electrode in theory. In light of these facts, we choose a counterpart crystalline material to substitute our amorphous Rh(OH)₃ for configuration of the computational model as the amorphous ones are acknowledged to be short-range ordered [54]. Since the amorphous rhodium oxide hydrate (Rh(OH)₃ or Rh₂O₃·3H₂O) will lose crystal water molecular and be converted to the crystalline Rh₂O₃ (JCPDS No. 76-0148, R-3c) when the annealing temperature is increased to 900 °C (Figs. S18 and S19d) [39,40], the crystalline Rh₂O₃ (R-3c) with one crystal water molecule (i.e. Rh₂O₃·H₂O) was chosen to simulate the a-Rh(OH)₃ for DFT calculation. Furthermore, the surface energies of different crystal planes of NiTe and a-Rh(OH)₃ were calculated as well (Fig. S44, Tables S9 and Table S10), among which the surface energy of NiTe (110) plane is the lowest one (Fig. S44, Table S9), which is in line with the HRTEM image and SAED patterns (Figs. 1f and S22). As for the a-Rh(OH)₃, the crystalline Rh₂O₃·H₂O is adopted to approximately simulate it and calculate the surface energy. Similarly, the surface energy of Rh₂O₃·H₂O (310) plane is the lowest one, which seems to be possible to combine with NiTe (110) for DFT calculation. We notice that although the surface energies of NiTe (110) and Rh₂O₃·H₂O (310) are the counterpart two lowest ones and the angle θ between the lattice parameters of them is the same and equal to 90° (Tables S7 and S8); however, their lattice mismatch rate is up to over 5%. Thus, we have to consider other factors besides surface energy for constructing a heterojunction model. To ensure the lattice mismatch rate is less than 5%, it is necessary to expand the cell according to the least common multiple of the lattice parameters of NiTe (110) and Rh₂O₃·H₂O (310). Unfortunately, after cell expansion, the number of atoms of 14 × 19 NiTe (110) supercell and 5 × 7 Rh₂O₃·H₂O (310) supercell is far beyond capability for DFT calculation. Noteworthy, in addition to NiTe (110) and

Rh₂O₃·H₂O (110) planes, we tried our best to consider and calculate most of the combination cases of NiTe and Rh₂O₃·H₂O. Also, other crystal planes such as (111), (321) and (121) of Rh₂O₃·H₂O with low surface energy have the same problem, i.e. their lattice mismatch is larger than 5% or their atoms model are far beyond the capability for DFT calculation after cell expansion (Table S10).

Impressively, the lattice mismatch is only 1% (much smaller than 5%) when a 2 × 2 NiTe (110) supercell ($a = 10.55596 \text{ \AA}$, $b = 13.946612 \text{ \AA}$) is coupled with a 2 × 1 Rh₂O₃·H₂O (110) supercell ($a = 10.4203 \text{ \AA}$, $b = 14.0898 \text{ \AA}$) to construct a heterostructure of Rh₂O₃·H₂O/NiTe, being suitable as a configured atomic model for a-Rh(OH)₃/NiTe. The optimized structural models are shown in Figs. 6a and S45, which fully meets the requirements for DFT calculations. For the sake of consistency, Rh₂O₃·H₂O/NiTe is labeled as a-Rh(OH)₃/NiTe herein after. It is well known that electron transfer could be occurred when a heterostructure was formed between two different materials [23], the reason of which could be attributed to the different electronegativity of the atoms. Since the electronegativity of Rh, O, Ni and Te are 2.28, 3.44, 1.91 and 2.10 in our case (Fig. 6a), the electrons should be redistributed. As shown in Fig. 6b, charge density area is enlarged along the a-Rh(OH)₃/NiTe interface. Particularly, the charges are accumulated around the Rh and O atoms but are depleted on Ni and Te atoms at the interfacial region, suggesting that the charges were transferred from Ni and Te to Rh and O (Fig. 6b), being consistent with the XPS results [56,57]. The planar-averaged charge density difference along the Z direction is shown in Fig. S45, further confirming that the electrons are mainly transferred from NiTe to a-Rh(OH)₃ through the interface [57]. In order to quantify the transferred charges, Bader charge analysis was performed, which signifies that ca. 3.04 *e* charges were transferred from NiTe to a-Rh(OH)₃ at the interface. In light of the fact that a locally-enhanced electronic field with irregular shape area around the Rh sites was generated, it suggests that the a-Rh(OH)₃/NiTe heterostructure could offer more free electrons to promote the absorption of H_{ads} and subsequently facilitate H₂ evolution [56].

Furthermore, the projected-density of states (PDOS) of NiTe and a-Rh(OH)₃/NiTe were further calculated (Fig. 6c and d). Compared with the pure NiTe, higher occupation near the Fermi level is observed for a-Rh(OH)₃/NiTe, indicating fast electron transfer and high conductivity of a-Rh(OH)₃/NiTe. As shown in Fig. 6c, the DOS (total) of a-Rh(OH)₃/NiTe and NiTe near the Fermi level is derived from the *d* orbitals rather than the *s* and *p* orbitals [58,59]. In contrast to the case of NiTe, the DOS of a-Rh(OH)₃/NiTe increases significantly near the Fermi level due to the extra contribution from Rh *d* orbitals of a-Rh(OH)₃ (Fig. 6d). This further confirms that the NiTe nanorod coupled with amorphous Rh(OH)₃ can remarkably improve the total *d*-electron domination of the catalyst near the Fermi level, which would be in favor of water activation and then lead to a high catalytic activity [8,56].

To understand the relationship between electronic structure and the enhanced HER activity, the reaction barrier for HER is further calculated, for which it includes the H₂O adsorption energy and the subsequent conversion energy of H_{ads} to H₂. The calculated results show that the a-Rh(OH)₃/NiTe heterostructure possess a substantially more negative ΔE_{H_2O} value than that of the pure NiTe (−1.018 eV vs. −0.303 eV) (Fig. 6e, left), signifying that the a-Rh(OH)₃/NiTe offers a favorable adsorption. This feature is beneficial for capturing H₂O molecules and facilitates the Volmer process [60], being consistent with the aforementioned hydrophilicity results (Fig. S37). In addition to ΔE_{H_2O} , the adsorption free energy of water (ΔG_{H_2O}) on the prepared catalysts are presented as well (Fig. 6e, Right). Since Rh site in a-Rh(OH)₃/NiTe has a much lower ΔG_{H_2O} than the Ni site in NiTe and a-Rh(OH)₃/NiTe, it indicates that the water molecule tends to absorb on the Rh site in a-Rh(OH)₃/NiTe, allowing the following step to generate adsorbed H atoms [61].

The adsorption free energy of hydrogen (ΔG_{H^+}) of the electrocatalyst is a descriptor to evaluate the HER catalytic activity. Ideally, a promising

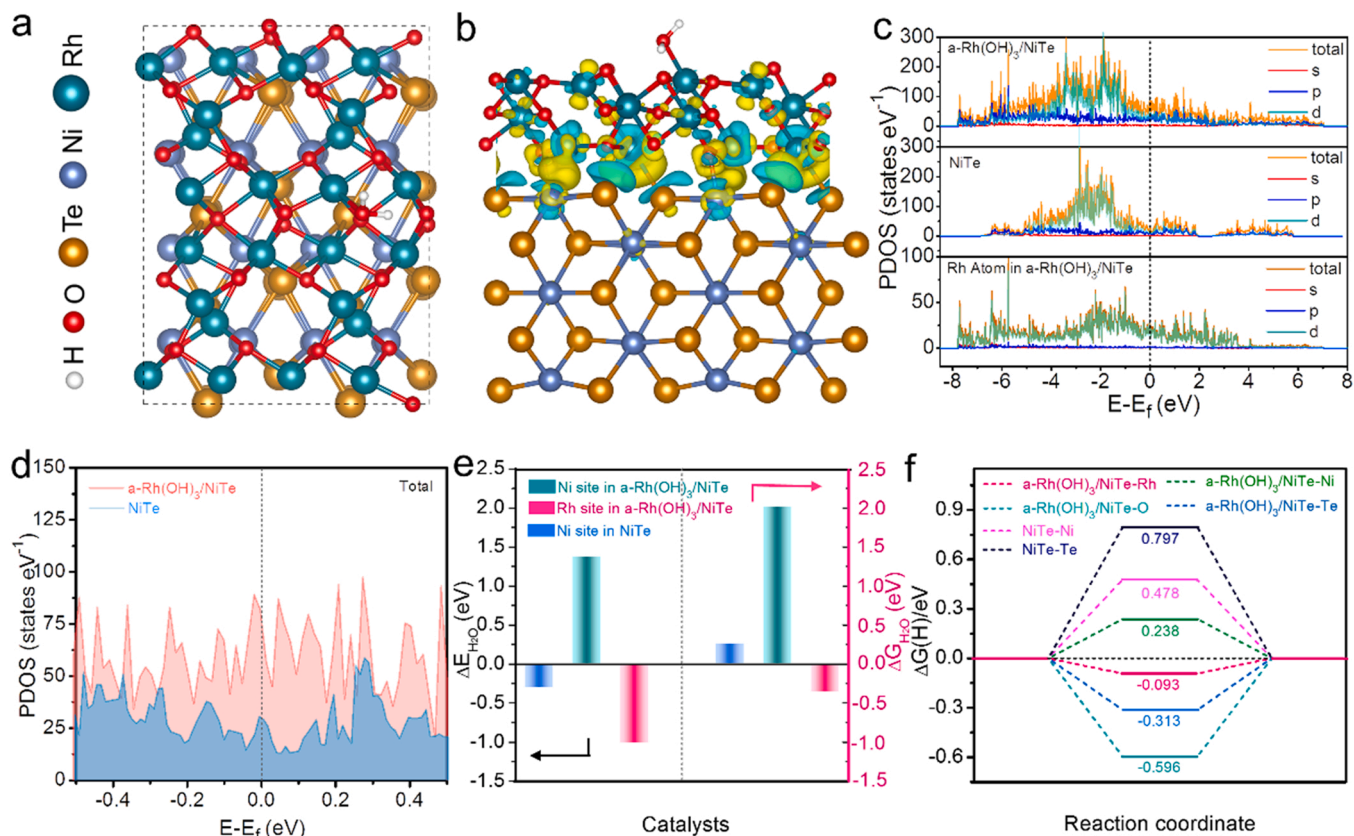


Fig. 6. DFT calculations. a) The top (a) views of the optimized structure of H* adsorbed on a-Rh(OH)₃/NiTe (110) plane. The steel-blue, dark-orange, black green, red and white balls symbolize Ni, Te, Rh, O and H atoms, respectively. b) Isosurface of the local charge density variation of a-Rh(OH)₃/NiTe, in which the yellow color means electron accumulation and the blue color indicates electron depletion. c) Calculated PDOS of a-Rh(OH)₃/NiTe and NiTe, with aligned Fermi level. d) Projected DOS of a-Rh(OH)₃/NiTe and NiTe. e) The adsorption energy of water H₂O (ΔE_{H_2O}) and the adsorption free energy of water (ΔG_{H_2O}) on a-Rh(OH)₃/NiTe and NiTe surface. f) Free energy diagram of the HER at equilibrium potential for various active sites of the catalyst.

catalyst should reveal a near-optimal hydrogen adsorption ($\Delta G_{H^*} = 0$), which can balance the reaction-barriers of the adsorption and desorption steps. Considering that the Ni, Te, Rh and O are all the potential active sites, all possible absorption cases are considered in this work (Fig. S46). The ΔG_{H^*} of NiTe (110) surface is first calculated as the reference, of which the ΔG_{H^*} at [Ni] and [Te] site are 0.478 eV and 0.797 eV, respectively, suggesting that the H_{ads} tends to be adsorbed on the [Ni] sites in NiTe (Fig. 6f). It should be noted that the ΔG_{H^*} values of NiTe are positive and far away from the optimal $\Delta G_{H^*} = 0$, suggesting that NiTe has weak adsorption feature for hydrogen and possess a slow HER reaction kinetics, which is consistent with its addressed poor catalytic activity [23]. In terms of a-Rh(OH)₃/NiTe, the ΔG_{H^*} values at [Ni], [Te], [Rh] and [O] sites are calculated to be 0.238, −0.313, −0.093 and −0.596 eV, respectively, demonstrating that the ΔG_{H^*} at [Ni] and [Te] sites is optimized after coupling with a-Rh(OH)₃ layers. Furthermore, we also calculated the ΔG_{H^*} at [O] sites in a-Rh(OH)₃/NiTe and Rh₂O₃/NiTe. As shown in Fig. S48d, they are all quite negative, signifying that O sites have strong hydrogen adsorption capability and could impede the H₂ evolution. On the contrary, the value of ΔG_{H^*} at [Rh] site is reduced to 0.093 eV in a-Rh(OH)₃/NiTe as compared with the case of Rh₂O₃/NiTe, being much close to the optimal ΔG_{H^*} of an ideal HER catalyst, evidencing the fact that [Rh] sites in a-Rh(OH)₃/NiTe should act as main factor for the advanced HER catalytic activity. Consequently, we can conclude that the amorphous Rh(OH)₃ shell provides the main active sites for HER activity, while the crystalline rod-like core of NiTe with superior conductivity serves as a co-working catalyst that facilitates charge transfer and promotes the release of the produced H₂.

4. Conclusions

In conclusion, a novel core-shell nanorod array with amorphous Rh(OH)₃ and crystalline NiTe has been developed for pH-universal HER application via a facile two-step process. To reach a current density of 100 mA cm^{−2}, only 51, 109, and 64 mV overpotentials are required for HER in alkaline, neutral and acidic mediums, respectively, outperforming most of the recently reported advanced noble metal catalysts. The experiments and density functional theory calculations have revealed that the high catalytic performance is accredited to the coupling synergy of amorphous shell and the crystalline rod-like core. More specifically, the amorphous Rh(OH)₃ shell provides abundant active sites promoting reactants adsorption and the crystalline NiTe nanorod core possesses excellent conductivity facilitating the electron transfer. The addressed remarkable pH-Universal HER activity should also be attributed to its superhydrophilicity and aerophobicity features, which not only facilitates the access to electrolytes but also accelerates the release of the generated gas bubbles. The insights gained in this work from the multiscale viewpoint, including molecular and electronic behavior as well as mesoscopic level, are anticipated to provide a different angle for the design of high-performance HER electrodes.

CRediT authorship contribution statement

Huachuan Sun: Investigation, Writing – review & editing. **Linfeng Li:** Investigation. **Muhammad Humayun:** Investigation. **Huaming Zhang:** Investigation. **Yanan Bo:** Investigation. **Xiang Ao:** Investigation. **Xuefei Xu:** Investigation. **Kun Chen:** Investigation. **Kostya (Ken) Ostrikov:** Investigation. **Kaifu Huo:** Investigation. **Wenjun Zhang:**

Investigation. **Chundong Wang:** Supervision, Conceptualization, Writing – review & editing. **Yujie Xiong:** Supervision, Conceptualization, Writing – review & editing.

Declaration of Competing Interest

There is no any conflict-of-interest.

Acknowledgements

This work is financially supported by the National Key R&D Program of China (Grant No. 2017YFE0120500), the National Natural Science Foundation of China (Grants No. 51972129, 21725102), the South Xinjiang Innovation and Development Program of Key Industries of Xinjiang Production and Construction Corps (Grants No. 2020DB002), the Key Research and Development Program of Hubei (Grant No. 2020BAB079), the Fundamental Research Funds for the Central Universities (2019KFYXMBZ076), C.D.W. acknowledges the Hubei “Chu-Tian Young Scholar” Program.

Appendix A. Supporting information

Supplementary data associated with this article can be found in the online version at [doi:10.1016/j.apcatb.2022.121088](https://doi.org/10.1016/j.apcatb.2022.121088).

References

- [1] N.T. Suen, S.F. Hung, Q. Quan, N. Zhang, Y.J. Xu, H.M. Chen, Electrocatalysis for the oxygen evolution reaction: recent development and future perspectives, *Chem. Soc. Rev.* 46 (2017) 337, <https://doi.org/10.1039/C6CS00328A>.
- [2] Z.W. Seh, J. Kibsgaard, C.F. Dickens, I. Chorkendorff, J.K. Nørskov, T.F. Jaramillo, Combining theory and experiment in electrocatalysis: Insights into materials design, *Science* 355 (2017) 146, <https://doi.org/10.1126/science.aad4998>.
- [3] J.A. Turner, Sustainable hydrogen production, *Science* 305 (2004) 972, <https://doi.org/10.1126/science.1103197>.
- [4] J. Greeley, T.F. Jaramillo, J. Bonde, I. Chorkendorff, J.K. Nørskov, Computational high-throughput screening of electrocatalytic materials for hydrogen evolution, *Nat. Mater.* 5 (2006) 909–913, <https://doi.org/10.1038/nmat1752>.
- [5] I. Roger, M.A. Shipman, M.D. Symes, Earth-abundant catalysts for electrochemical and photoelectrochemical water splitting, *Nat. Rev. Chem.* 1 (2017) 0003, <https://doi.org/10.1038/s41570-016-0003>.
- [6] J. Shan, Y. Zheng, B. Shi, K. Davey, S.Z. Qiao, Regulating electrocatalysts via surface and interface engineering for acidic water electrooxidation, *ACS Energy Lett.* 4 (2019) 2719–2730, <https://doi.org/10.1021/acsenergylett.9b01758>.
- [7] D. Liu, X. Li, S. Chen, H. Yan, C. Wang, C. Wu, Y.A. Haleem, S. Duan, J. Lu, B. Ge, P. M. Ajayan, Y. Luo, J. Jiang, L. Song, Atomically dispersed platinum supported on curved carbon supports for efficient electrocatalytic hydrogen evolution, *Nat. Energy* 4 (2019) 512–518, <https://doi.org/10.1038/s41560-019-0402-6>.
- [8] J. Zhang, Y. Zhao, X. Guo, C. Chen, C.-L. Dong, R.-S. Liu, C.-P. Han, Y. Li, Y. Gogotsi, G. Wang, Single platinum atoms immobilized on an MXene as an efficient catalyst for the hydrogen evolution reaction, *Nat. Catal.* 1 (2018) 985–992, <https://doi.org/10.1038/s41929-018-0195-1>.
- [9] X. Wang, Y. Zheng, W. Sheng, Z.J. Xu, M. Jaroniec, S.Z. Qiao, Strategies for design of electrocatalysts for hydrogen evolution under alkaline conditions, *Mater. Today* 36 (2020) 125–138, <https://doi.org/10.1016/j.mattod.2019.12.003>.
- [10] X. Wang, C. Xu, M. Jaroniec, Y. Zheng, S.Z. Qiao, Anomalous hydrogen evolution behavior in high-pH environment induced by locally generated hydronium ions, *Nat. Commun.* 10 (2019) 4876, <https://doi.org/10.1038/s41467-019-12773-7>.
- [11] Y.-L. Zhu, Q. Lin, Y.-J. Zhong, H.A. Tahini, Z.P. Shao, H.T. Wang, Metal oxide-based materials as an emerging family of hydrogen evolution electrocatalysts, *Energy Environ. Sci.* 13 (2020) 3361, <https://doi.org/10.1039/D0EE02485F>.
- [12] Y. Li, Z. Dong, L.J. Jiao, Multifunctional transition metal-based phosphides in energy-related electrocatalysis, *Adv. Energy Mater.* 10 (2020), 1902104, <https://doi.org/10.1002/aenm.201902104>.
- [13] B. Zhang, L. Zhang, Q. Tan, J. Wang, J. Liu, H. Wan, L. Miao, J. Jiang, Simultaneous interfacial chemistry and inner Helmholtz plane regulation for superior alkaline hydrogen evolution, *Energy Environ. Sci.* 13 (2020) 3007–3013, <https://doi.org/10.1039/D0EE02020F>.
- [14] C.D. Wang, Y. Tian, Y. Gu, K.H. Xue, H.C. Sun, X. Miao, L. Dai, Plasma-induced moieties impart super-efficient activity to hydrogen evolution electrocatalysts, *Nano Energy* 85 (2021), 106030, <https://doi.org/10.1016/j.nanoen.2021.106030>.
- [15] J. Wang, Z. Zhang, H. Song, B. Zhang, J. Liu, X. Shai, L. Miao, Water dissociation kinetic-oriented design of nickel sulfides via tailored dual sites for efficient alkaline hydrogen evolution, *Adv. Funct. Mater.* 31 (2020), 2008578, <https://doi.org/10.1002/adfm.202008578>.
- [16] A. Chunduri, S. Gupta, O. Bapat, A. Bhide, R. Fernandes, M.K. Patel, V. Bambole, A. Miotello, N. Patel, A unique amorphous cobalt-phosphide-boride bifunctional electrocatalyst for enhanced alkaline water-splitting, *Appl. Catal. B Environ.* 259 (2019), 118051, <https://doi.org/10.1016/j.apcatb.2019.118051>.
- [17] Z. Kou, L. Zhang, Y. Ma, X. Liu, W. Zang, J. Zhang, S. Huang, Y. Du, A.K. Cheetham, J. Wang, 2D carbide nanomeshes and their assembling into 3D microflow for efficient water splitting, *Appl. Catal. B Environ.* 243 (2019) 678–685, <https://doi.org/10.1016/j.apcatb.2018.11.008>.
- [18] Z. Xu, S. Jin, M.H. Seo, X. Wang, Hierarchical Ni-Mo₂C/N-doped carbon Mott-Schottky array for water electrolysis, *Appl. Catal. B Environ.* 292 (2021), 120168, <https://doi.org/10.1016/j.apcatb.2021.120168>.
- [19] Y. Zhu, H.-C. Chen, C.-S. Hsu, T.-S. Lin, C.-J. Chang, S.-C. Chang, L.-D. Tsai, H. M. Chen, Operando unraveling of the structural and chemical stability of P-substituted CoSe₂ electrocatalysts toward hydrogen and oxygen evolution reactions in alkaline electrolyte, *ACS Energy Lett.* 4 (2019) 987–994, <https://doi.org/10.1021/acsenergylett.9b00382>.
- [20] H. Sun, J.-G. Li, L. Lv, Z. Li, X. Ao, C. Xu, X. Xue, G. Hong, C. Wang, Engineering hierarchical CoSe₂/NiFe layered-double-hydroxide nanoarrays as high efficient bifunctional electrocatalyst for overall water splitting, *J. Power Sources* 425 (2019) 138–146, <https://doi.org/10.1016/j.jpowsour.2019.04.014>.
- [21] G. Zhao, Y. Jiang, S.-X. Dou, W. Sun, H. Pan, Interface engineering of heterostructured electrocatalysts towards efficient alkaline hydrogen electrocatalysis, *Sci. Bull.* 66 (2021) 85–96, <https://doi.org/10.1016/j.scib.2020.09.014>.
- [22] J. Mahmood, F. Li, S.M. Jung, M.S. Okyay, I. Ahmad, S.J. Kim, N. Park, H.Y. Jeong, J.B. Baek, An efficient and pH-universal ruthenium-based catalyst for the hydrogen evolution reaction, *Nat. Nanotechnol.* 12 (2017) 441, <https://doi.org/10.1038/nnano.2016.304>.
- [23] H. Sun, J.-M. Yang, J.-G. Li, Z. Li, X. Ao, Y.-Z. Liu, Y. Zhang, Y. Li, C. Wang, J. Tang, Synergistic coupling of NiTe nanoarrays with RuO₂ and NiFe-LDH layers for high-efficiency electrochemical-/photovoltage-driven overall water splitting, *Appl. Catal. B Environ.* 272 (2020), 118988, <https://doi.org/10.1016/j.apcatb.2020.118988>.
- [24] Q. Wang, M. Ming, S. Niu, Y. Zhang, G. Fan, J.S. Hu, Scalable solid-state synthesis of highly dispersed uncapped metal (Rh, Ru, Ir) nanoparticles for efficient hydrogen evolution, *Adv. Energy Mater.* 8 (2018) 1801691–1801698, <https://doi.org/10.1002/aenm.201801698>.
- [25] S. Cherevko, S. Geiger, O. Kasian, N. Kulyk, J.P. Grote, A. Savaş, Oxygen and hydrogen evolution reactions on Ru, RuO₂, Ir, and IrO₂ thin film electrodes in acidic and alkaline electrolytes: A comparative study on activity and stability, *Catal. Today* 262 (2016) 170, <https://doi.org/10.1016/j.cattod.2015.08.014>.
- [26] B. Shang, X. Cui, L. Jiao, K. Qi, Y. Wang, J. Fan, Y. Yue, H. Wang, Q. Bao, X. Fan, Lattice-mismatch-induced ultrastable 1T-phase MoS₂-Pd/Au for plasmon-enhanced hydrogen evolution, *Nano Lett.* 19 (2019) 2758, <https://doi.org/10.1021/acs.nanolett.8b04104>.
- [27] Z. Wu, Y. Zhao, H. Wu, Y. Gao, Z. Chen, W. Jin, J. Wang, T. Ma, L. Wang, Corrosion engineering on iron foam toward efficiently electrocatalytic overall water splitting powered by sustainable energy, *Adv. Funct. Mater.* 31 (2021), 2010437, <https://doi.org/10.1002/adfm.202010437>.
- [28] D. Cao, J. Wang, H. Xu, D. Cheng, Growth of highly active amorphous rucuo nanosheets on cu nanotubes for the hydrogen evolution reaction in wide pH values, *Small* 16 (2020), e2000924, <https://doi.org/10.1002/sml.202000924>.
- [29] H. Sun, W. Zhang, J.-G. Li, Z. Li, X. Ao, K.-H. Xue, K.K. Ostrikov, J. Tang, C. Wang, Rh-engineered ultrathin NiFe-LDH nanosheets enable highly-efficient overall water splitting and urea electrolysis, *Appl. Catal. B Environ.* 284 (2021), 119740, <https://doi.org/10.1016/j.apcatb.2020.119740>.
- [30] J. Wang, L. Han, B. Huang, Q. Shao, H.L. Xin, X. Huang, Amorphization activated ruthenium-tellurium nanorods for efficient water splitting, *Nat. Commun.* 10 (2019) 5692, <https://doi.org/10.1038/s41467-019-13519-1>.
- [31] Y. Zhou, H.J. Fan, Progress and challenge of amorphous catalysts for electrochemical water splitting, *ACS Mater. Lett.* 3 (2020) 136–147, <https://doi.org/10.1021/acsmateriale.0c00502>.
- [32] H.B. Li, M.H. Yu, F.X. Wang, P. Liu, Y. Liang, J. Xiao, C.X. Wang, Y.X. Tong, G. W. Yang, Amorphous nickel hydroxide nanospheres with ultrahigh capacitance and energy density as electrochemical pseudocapacitor materials, *Nat. Commun.* 4 (2013) 1894, <https://doi.org/10.1038/ncomms2932>.
- [33] E.J.M. O'Sullivan, L.D. Burke, Kinetics of oxygen gas evolution on hydrous rhodium oxide films, *J. Electrochem. Soc.* 137 (1990) 466–471, <https://doi.org/10.1149/1.2086464>.
- [34] C. Guo, Y. Shi, S. Lu, Y. Yu, B. Zhang, Amorphous nanomaterials in electrocatalytic water splitting, *Chin. J. Catal.* 42 (2021) 1287–1296, [https://doi.org/10.1016/S1872-2067\(20\)63740-8](https://doi.org/10.1016/S1872-2067(20)63740-8).
- [35] B. Zhang, J. Liu, J. Wang, Y. Ruan, X. Ji, K. Xu, C. Chen, H. Wan, L. Miao, J. J. Jiang, Interface engineering: The Ni(OH)₂/MoS₂ heterostructure for highly efficient alkaline hydrogen evolution, *Nano Energy* 37 (2017) 74–80, <https://doi.org/10.1016/j.nanoen.2017.05.011>.
- [36] Y. Hu, G. Luo, L. Wang, X. Liu, Y. Qu, Y. Zhou, F. Zhou, Z. Li, Y. Li, T. Yao, C. Xiong, B. Yang, Z. Yu, Y. Wu, Single Ru atoms stabilized by hybrid amorphous/crystalline FeCoNi layered double hydroxide for ultraefficient oxygen evolution, *Adv. Energy Mater.* 11 (2020), 202002816, <https://doi.org/10.1002/aenm.202002816>.
- [37] X. Yu, Z.Y. Yu, X.L. Zhang, Y.R. Zheng, Y. Duan, Q. Gao, R. Wu, B. Sun, M.R. Gao, G. Wang, S.H. Yu, “Superaerophobic” nickel phosphide nanoarray catalyst for efficient hydrogen evolution at ultrahigh current densities, *J. Am. Chem. Soc.* 141 (2019) 7537–7543, <https://doi.org/10.1021/jacs.9b02527>.
- [38] X. Liu, M. Gong, S. Deng, T. Zhao, T. Shen, J. Zhang, D. Wang, Transforming damage into benefit: corrosion engineering enabled electrocatalysts for water splitting, *Adv. Funct. Mater.* 31 (2020), 2009032, <https://doi.org/10.1002/adfm.202009032>.

- [39] A. Ari, S. Popovi, R. Trojko, S. Musi, The thermal behavior of amorphous rhodium hydrous oxide, *J. Alloy. Compd.* 320 (2001) 140–148, [https://doi.org/10.1016/S0925-8388\(01\)00938-0](https://doi.org/10.1016/S0925-8388(01)00938-0).
- [40] A. Ari, S. Popovi, S. Musi, Formation of crystalline phases by thermal treatment of amorphous rhodium hydrous oxide, *Mater. Lett.* 55 (2002) 145–151, [https://doi.org/10.1016/S0167-577X\(01\) 00637-1](https://doi.org/10.1016/S0167-577X(01) 00637-1).
- [41] S. Musić, A. Šarić, S. Popović, M. Ivanda, Formation and characterisation of nanosize α -Rh₂O₃ particles, *J. Mol. Struct.* 924–926 (2009) 221–224, <https://doi.org/10.1016/j.molstruc.2008.10.017>.
- [42] Z. Xue, X. Li, Q. Liu, M. Cai, K. Liu, M. Liu, Z. Ke, X. Liu, G. Li, Interfacial electronic structure modulation of NiTe nanoarrays with NiS Nanodots facilitates electrocatalytic oxygen evolution, *Adv. Mater.* 31 (2019), e1900430, <https://doi.org/10.1002/adma.201900430>.
- [43] K. Zhu, J. Chen, W. Wang, J. Liao, J. Dong, M.O.L. Chee, N. Wang, P. Dong, P. M. Ajayan, S. Gao, J. Shen, M. Ye, Etching-doping sedimentation equilibrium strategy: accelerating kinetics on hollow Rh-doped CoFe-layered double hydroxides for water splitting, *Adv. Funct. Mater.* 30 (2020), 2003556, <https://doi.org/10.1002/adfm.202003556>.
- [44] L. Yang, H. Xu, H. Liu, D. Cheng, D. Cao, Active site identification and evaluation criteria of in situ grown CoTe and NiTe nanoarrays for hydrogen evolution and oxygen evolution reactions, *Small Methods* 3 (2019), 1900113, <https://doi.org/10.1002/smt.201900113>.
- [45] Z. Wang, L. Zhang, In situ growth of NiTe nanosheet film on nickel foam as electrocatalyst for oxygen evolution reaction, *Electrochem. Commun.* 88 (2018) 29–33, <https://doi.org/10.1016/j.elecom.2018.01.014>.
- [46] A. Sb, X.B. Miao, C.B. Tao, A. Kc, X.B. Yong, X.Q. Huang, Surface engineering of RhOOH nanosheets promotes hydrogen evolution in alkaline, *Nano Energy* 78 (2020), 105224, <https://doi.org/10.1016/j.nanoen.2020.105224>.
- [47] H. Wang, Y. Xia, H. Li, X. Wang, Y. Yu, X. Jiao, D. Chen, Highly active deficient ternary sulfide photoanode for photoelectrochemical water splitting, *Nat. Commun.* 11 (2020) 3078, <https://doi.org/10.1038/s41467-020-16800-w>.
- [48] T. Reier, Z. Pawolek, S. Cherevko, M. Bruns, T. Jones, D. Teschner, S. Selve, A. Bergmann, N.N. Hong, R. Schloegl, Molecular insight in structure and activity of highly efficient, low-Ir Ir-Ni oxide catalysts for electrochemical water splitting (OER), *J. Am. Chem. Soc.* 137 (2015) 13031–13040, <https://doi.org/10.1021/jacs.5b07788>.
- [49] J. Wang, B. Huang, Y. Ji, M. Sun, T. Wu, R. Yin, X. Zhu, Y. Li, Q. Shao, X. Huang, A general strategy to glassy M-Te (M = Ru, Rh, Ir) porous nanorods for efficient electrochemical N₂ fixation, *Adv. Mater.* 32 (2020), e1907112, <https://doi.org/10.1002/adma.201907112>.
- [50] H. Li, S. Chen, Y. Zhang, Q. Zhang, X. Jia, Q. Zhang, L. Gu, X. Sun, L. Song, X. Wang, Systematic design of superaerophobic nanotube-array electrode comprised of transition-metal sulfides for overall water splitting, *Nat. Commun.* 9 (2018) 2452, <https://doi.org/10.1038/s41467-018-04888-0>.
- [51] X. Shan, J. Liu, H. Mu, Y. Xiao, B. Mei, W. Liu, G. Lin, Z. Jiang, L. Wen, L. Jiang, An engineered superhydrophilic/superaerophobic electrocatalyst composed of the supported CoMoS_x chalcogel for overall water splitting, *Angew. Chem. Int. Ed.* 59 (2020) 1659–1665, <https://doi.org/10.1002/anie.201911617>.
- [52] Y. Li, H. Zhang, T. Xu, Z. Lu, X. Wu, P. Wan, X. Sun, L. Jiang, Under-water superaerophobic pine-shaped Pt nanoarray electrode for ultrahigh-performance hydrogen evolution, *Adv. Funct. Mater.* 25 (2015) 1737–1744, <https://doi.org/10.1002/adfm.201404250>.
- [53] Y. Li, X. Tan, H. Tan, H. Ren, S. Chen, W. Yang, S.C. Smith, C. Zhao, Phosphine vapor-assisted construction of heterostructured Ni₂P/NiTe₂ catalysts for efficient hydrogen evolution, *Energy Environ. Sci.* 13 (2020) 1799–1807, <https://doi.org/10.1039/D0EE00666A>.
- [54] N. Chen, Y.-X. Du, G. Zhang, W.-T. Lu, F.-F. Cao, Amorphous nickel sulfoselenide for efficient electrochemical urea-assisted hydrogen production in alkaline media, *Nano Energy* 81 (2021), 105605, <https://doi.org/10.1016/j.nanoen.2020.105605>.
- [55] Y. Zhang, B. Ouyang, J. Xu, G. Jia, S. Chen, R.S. Rawat, H.J. Fan, Rapid synthesis of cobalt nitride nanowires: highly efficient and low-cost catalysts for oxygen evolution, *Angew. Chem. Int. Ed.* 55 (2016) 8670–8674, <https://doi.org/10.1002/anie.201604372>.
- [56] K.L. Zhou, Z. Wang, C.B. Han, X. Ke, C. Wang, Y. Jin, Q. Zhang, J. Liu, H. Wang, H. Yan, Platinum single-atom catalyst coupled with transition metal/metal oxide heterostructure for accelerating alkaline hydrogen evolution reaction, *Nat. Commun.* 12 (2021) 3783, <https://doi.org/10.1038/s41467-021-24079-8>.
- [57] J.J. Liu, B. Cheng, J.G. Yu, A new understanding of the photocatalytic mechanism of the direct Z-scheme g-C₃N₄/TiO₂ heterostructure, *Phys. Chem. Chem. Phys.* 18 (2016) 31175, <https://doi.org/10.1039/C6CP06147H>.
- [58] X. Meng, C. Ma, L. Jiang, R. Si, X. Meng, Y. Tu, L. Yu, X. Bao, D. Deng, Distance synergy of MoS₂-confined rhodium atoms for highly efficient hydrogen evolution, *Angew. Chem. Int. Ed.* 59 (2020) 10502–10507, <https://doi.org/10.1002/anie.202003484>.
- [59] J. Yin, J. Jin, M. Lu, B. Huang, H. Zhang, Y. Peng, P. Xi, C.H. Yan, Iridium single atoms coupling with oxygen vacancies boosts oxygen evolution reaction in acid media, *J. Am. Chem. Soc.* 142 (2020) 18378–18386, <https://doi.org/10.1021/jacs.0c05050>.
- [60] J. Xu, T. Liu, J. Li, B. Li, Y. Liu, B. Zhang, D. Xiong, I. Amorim, W. Li, L. Liu, Boosting the hydrogen evolution performance of ruthenium clusters through synergistic coupling with cobalt phosphide, *Energy Environ. Sci.* 11 (2018) 1819–1827, <https://doi.org/10.1039/C7EE03603E>.
- [61] Y. Sun, Z. Xue, Q. Liu, Y. Jia, Y. Li, K. Liu, Y. Lin, M. Liu, G. Li, C.Y. Su, Modulating electronic structure of metal-organic frameworks by introducing atomically dispersed Ru for efficient hydrogen evolution, *Nat. Commun.* 12 (2021) 1369, <https://doi.org/10.1038/s41467-021-21595-5>.